Journal of Materials Chemistry A

Surface Engineered Angstrom Thick ZnO-sheathed TiO2 Nanowires as Photoanode for Performance Enhanced Dye-sensitized Solar Cells

Journal:	*Journal of Materials Chemistry A*
Manuscript ID:	TA-ART-07-2014-003445.R1
Article Type:	Paper
Date Submitted by the Author:	06-Aug-2014
Complete List of Authors:	Ulusoy, Turkan; Bilkent University, Materials Science and Nanotechnology Ghobadi, Amir; Bilkent University, Electrical and Electronics Engineering Okyay, Ali Kemal; Bilkent University, UNAM- Institute of Materials Science and Nanotechnology

Journal Name

RSCPublishing

ARTICLE

Surface Engineered Angstrom Thick ZnO-sheathed TiO_2 Nanowires as Photoanode for Performance Enhanced Dye-sensitized Solar Cells†

Cite this: DOI: 10.1039/x0xx00000x

Received 00th July 2014,
Accepted 00th July 2014

DOI: 10.1039/x0xx00000x

www.rsc.org/

T. G. Ulusoy[a,b], A. Ghobadi[a,c] and A. K. Okyay[a,b,c*]

This paper presents a systematic study on the impact of angstrom-thick atomic layer deposited (ALD) ZnO sheath on hydrothermally grown TiO_2 nanowires (NWs) used as photoanode in dye sensitized solar cells (DSSCs). We designed, synthesized and well-characterized the samples for different cycles of ZnO and compared their photovoltaic (PV) performance. Of particular interest is the optimum thickness of 2 cycles ZnO shell wrapping around TiO_2 NWs where device shows a jump in the efficiency by about 3-fold, compared to a control reference device. This paper contains results and features which demonstrate passivation of surface state traps upon deposition of ZnO shell. While this passivation of surface traps provides a reduction in the surface states mediated electrons' back-reactions (K^{trap}_{ET}), it is speculated that ZnO-induced surface band bending (SBB) adds a substantial reduction in recombination rate of the device via reducing the conduction band (CB) electrons' recombination rate (K^{CB}_{ET}). Moreover, an enhancement in the amount of dye uptake for ZnO-coated TiO_2 samples is ascertained and explained utilizing the isoelectric point (IEP) concept. In spite of excellent PV power conversion efficiencies displayed for first cycles of ZnO, thicker layers impede injection rate of electrons and reduce the efficiency of the device through capturing the photogenerated dye electrons by ZnO quantum well. Here we scrutinized the mechanisms contributing to this unprecedented change and it is correlated with enhancement in the device efficiency.

I. Introduction

With ever-increasing demand for renewable and clean energy in recent years, dye-sensitized solar cells (DSSCs)[1] have attracted much attention as a viable photovoltaic (PV) technology that could compete with Si based PV[2] thanks to its ease of fabrication and low manufacturing costs.[3–7] In order to increase the light harvesting efficiency of DSSCs, new organic dyes with higher extinction coefficients and broader absorption spectra are being investigated.[8–11] In addition, approaches that yield large surface area are utilized to further increase PV efficiency via higher dye loading. Colloidal crystalline nanoparticle based TiO_2 films that provide high surface area, are the most widely used type of photoanodes in DSSC technology. However, the disordered state hinders efficient charge transport in the TiO_2 film due to low effective charge carrier mobility and high carrier recombination rate. To improve charge transfer efficiency, one dimensional (1D) structures such as nanotubes and nanowires (NWs) are desirable since they provide higher mobility and lower recombination rate in addition to high surface area.[12–14] Moreover, hierarchical oxide nanostructures, which can provide high surface area for dye uptake and 1D highly branched structure for better light scattering and overall light conversion efficiency, has turned to a hot research topic in recent years.[15,16]

Recently, there is a rapidly growing interest among the DSSC community towards the optimization of the interfacial layer between dye and inorganic photoanode. Substantial improvement in DSSC performance could be attained by engineering the dye-TiO_2 interface in order to 1) reduce recombination of charge carriers by both passivation of surface state traps in the interface and retardation of photo-injected electrons' back–transfer from TiO_2 conduction band to the oxidized red-ox species, 2) increase injection yield and collection efficiency of photogenerated carriers from dye to TiO_2, 3) increase light absorption efficiency by enhancing the amount of dye uptake. Several studies show that high band-gap metal-oxide materials such as In_2O_3, ZrO_2, Al_2O_3, Nb_2O_5, Ga_2O_3 and SiO_2 could reduce recombination in DSSC by blocking back-transfer of electrons and hence barricade the recombination of electrons with either oxidized dye molecules or with the oxidized redox couple (the latter one is thought to be particularly dominant in device performance degradation),[17–22] or via reducing the density of surface trap states on TiO_2 surface.[18,23] Besides, some studies demonstrate that metal-oxides like Nb_2O_5, $SrTiO_3$, ZrO_2 and Al_2O_3 can contribute in device performance enhancement by inducing a surface dipole in

[a]UNAM – National Nanotechnology Research Center, Bilkent University, Ankara 06800, Turkey
[b]Institute of Materials Science and Nanotechnology, Bilkent University, Ankara 06800, Turkey
[c]Department of Electrical and Electronics Engineering, Bilkent University, Ankara 06800, Turkey
*Corresponding author (email): aokyay@ee.bilkent.edu.tr
† Electronic supplementary information (ESI) available: Fig.s S1–S6.

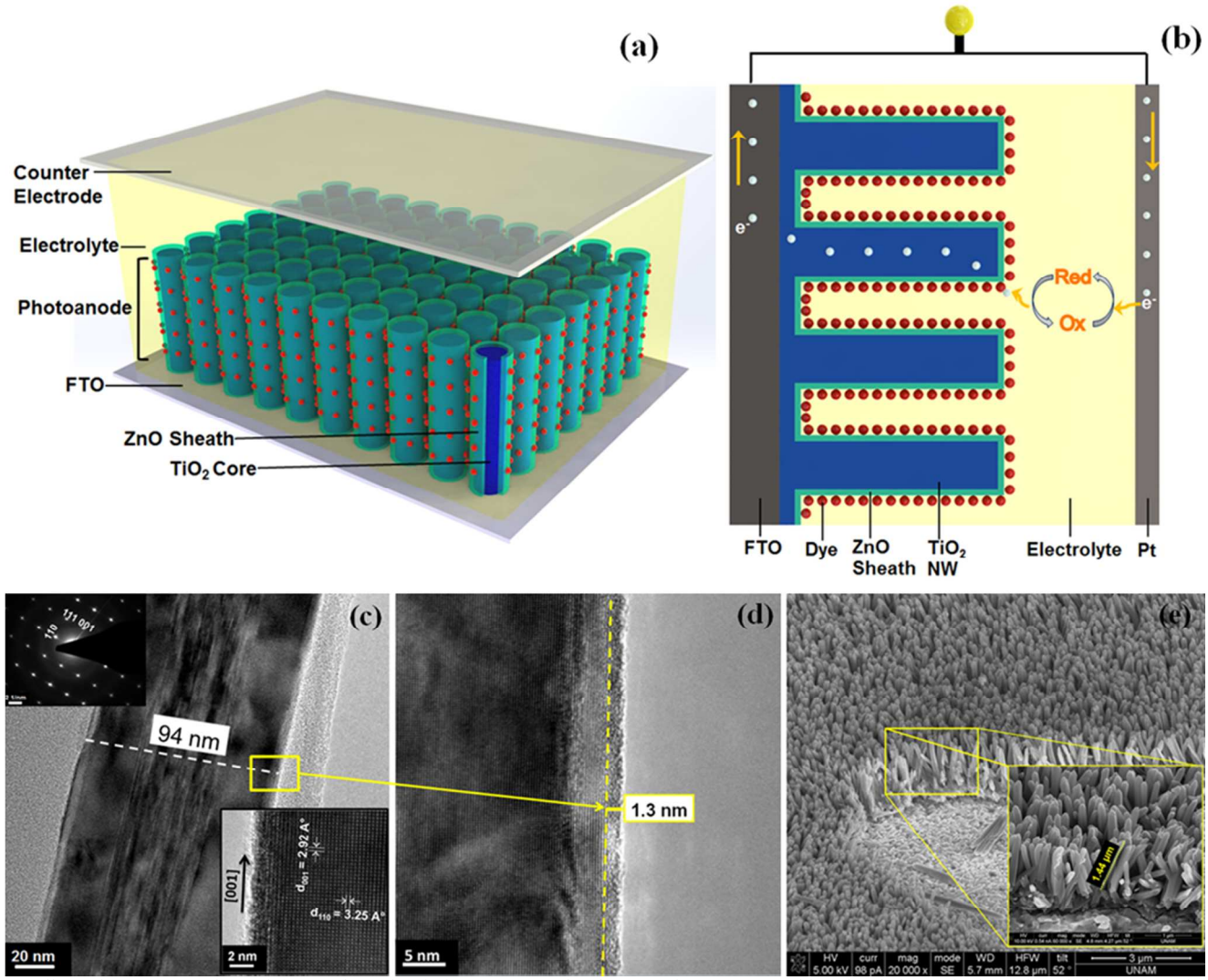

Fig. 1 Illustrative representations of a) 3D schematic of TiO_2-ZnO core-sheath composite structure and b) related electronic dynamics of electron transfer of the DSSC. (c) TEM and HRTEM images of 10 ALD cycles ZnO coated TiO_2 NWs (SAED pattern and HRTEM images in the inset proves the growth of a single crystalline rutile phase)(d) HRTEM image estimating the thickness of ZnO sheath layer to be 1.3 nm for 10 ALD cycles (e) SEM images (cross sectional) of densely packed TiO_2 NW arrays.

metal-oxide/dye interface which leads to a negative shift of TiO_2 conduction band[24] and enhancement in injection yield of photo-induced electrons.[25] In addition to improved electrodynamics at the interface, researchers in[22,24] explain device performance improvement to be related to dye adsorption enhancement. Materials such as ZnO, MgO, ZrO_2 and Al_2O_3 with high isoelectric point (IEP) compared to TiO_2 can provide more favorable host sites for carboxylic groups which allows higher amounts of dye uptake onto the surface of TiO_2 NWs coated with such materials as opposed to bare ones. The increased dye loading yields increased amount of light absorption. However, a serious drawback with most of the high band gap materials is that forward electron injection (dye to TiO_2) can be significantly impeded and electron injection efficiency could be totally diminished if the interfacial layer is merely a couple of nanometer thick. To tackle this problem, recently, researchers have proved that electron transfer rate could be systematically tailored proposing ultrathin tunneling layers by using a variety of coating methods. Dip-coating is one of these methods which has been commonly utilized to coat electrodes. [27,28] However, this technique typically shows non-uniform thicknesses as well as presence of pinholes on the surface which creates unwanted conduits for electron back transfer.[29] Contrary to this method, atomic layer deposition (ALD) technique, a self-limiting growth process, offers uniform and conformal coating of non-line-of-sight surfaces including high aspect ratio features (like dense micrometer long NWs as in our case). Although the ALD has lower cost effectiveness compared to other deposition techniques, it ensures uniform and conformal coating of a pinhole-free angstrom-thick metal-oxide layer through the whole substrate surface which is an imperative task to improve material/device performance especially in high aspect ratio features.[15,16,19,21] By taking all of these factors into consideration, this work aims to improve DSSC device performance by surface modification of hydrothermally grown TiO_2 NWs using sub-nanometer ALD-coated ZnO shell-like interfacial layer. It is shown that a composite photoanode formed by an optimized thickness of ZnO shell wrapping around TiO_2 NWs can provide a significant enhancement in PV performance of the DSSC device through reducing surface trap states on TiO_2 NWs as well as increasing dye

loading amount without hampering electron injection efficiency, which is the main trade-off in using high band gap metal-oxide coated NW based photoanodes.

II. Results and discussion

In order to investigate the effect of ZnO interfacial layer on PV performance of DSSC devices, hydrothermally grown TiO_2 photoanodes are coated with different ALD cycles of ZnO. 3D schematic of TiO_2-ZnO core-shell composite structure and related electronic dynamics of electron transfer process are depicted in Fig. 1. As presented in Fig. 1a and 1b, the proposed DSSC device consists of 4 main parts: 1) a composite photoanode formed by hydrothermally grown TiO_2 NWs on transparent conducting glass (FTO, F: SnO_2-doped, Tec 7Ω/sq) coated with conformal layer of sub-nanometer ZnO as a sheath. 2) cis-bis (isothiocyanato) bis (2,2′-bipyridyl-4,4′-dicarboxylato) ruthenium (II) (N719) as photosensitizer 3) the iodide/tri-iodide (I^-/I^{3-}) shuttle as electron transfer mediator and finally 4) Pt-coated conducting glass as counter electrode.

The morphology and structural characteristics of the composite photoanodes are investigated by scanning electron microscope (SEM, FEI-Quanta 200 FEG) and transmission electron microscope (TEM, FEI-Tecnai G2 F30). Fig. 1c and 1d shows TEM and SEM images of the densely packed TiO_2 NW arrays on FTO substrate, respectively. Fig. 1c displays the TEM image of NWs with diameter in a range of 80-100 nm. As evidenced by the sharp selected area electron diffraction (SAED) pattern of a NW examined along the [110] zone axis and high resolution TEM (HRTEM) image shown in the inset, NWs are single crystalline along their entire lengths having lattice fringes with interplanar spacings of d_{110} = 3.25 Å and d_{001} = 2.9 Å which are consistent with the rutile phase. The [110] axis is perpendicular to the NW side walls, and the NWs grow along the [001] direction. Also HRTEM image shown in Fig. 1d indicates that a 1.3 nm-thick 10 ALD cycles wurtzite ZnO (as confirmed in[30]) passivation layer is grown conformally on single crystalline TiO_2 NWs which yields a growth rate of 1.3 Å per cycle (below 10 cycles it is difficult to discern ZnO shell layer from TiO_2 core). It is worth noting that a reduced growth rate on samples with high density of NW arrays compared to planar surfaces (1.55 Å reported in[30]) is attributed to reduced diffusion of the gas precursor due to high aspect ratio. Also, SEM image reveals (Fig. 1e) that the NWs are approximately about 1.2-1.6 μm in length.

To identify the crystalline structure of the obtained samples and orientation of the grown NWs, X-ray diffraction (XRD PANALYTICAL, X'pert Multi-Purpose X-Ray Diffractometer (MPD) instrument) analysis is performed. XRD patterns are collected over the 2θ angular range of 20–80° using Bragg–Brentano geometry (Cu Kα). The spectra (Fig. 2) clearly reveal that the prepared TiO_2-ZnO core-shell samples' diffraction peaks are in accordance with a standard diffraction pattern of rutile structure of TiO_2 (JCPDS,82-0514) with the prominent rutile peak for (110) direction. The diffraction peaks of ZnO coated TiO_2 NWs are quite similar to those of the bare TiO_2 NWs. Moreover no peak associated with ZnO in the XRD spectra since the shell layer is ultrathin.

Further evidence for the existence of angstrom scale ZnO shell layer is obtained by high resolution X-ray photoelectron spectroscopy (XPS) measurement performed with a Thermo (K-Alpha Monochromated High-Performance XPS Spectrometer) instrument to monitor the TiO_2-ZnO interface formation and determine the surface elemental compositions. XPS spectra of the Ti2p and the Zn2p, which are shown in Fig. S1 (supplementary information), are taken on the surface of the core-sheath design. The energy scales of the spectra are calibrated by shifting the XPS signal

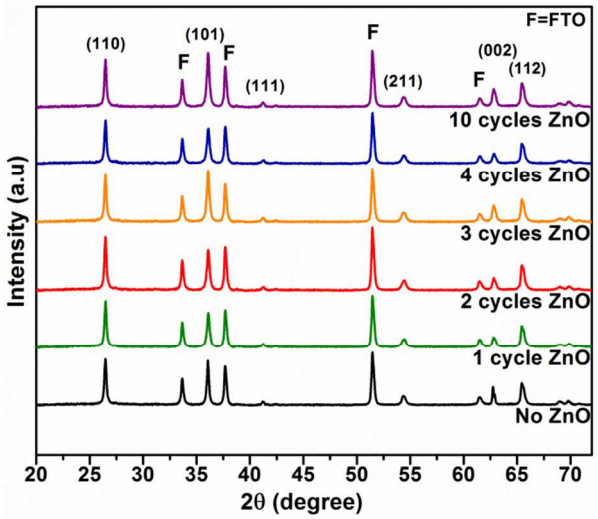

Fig. 2 XRD patterns of TiO_2-ZnO core-sheath composite structures for different ALD cycles of ZnO sheath layer. Diffraction peaks are in accordance with a standard diffraction pattern of rutile structure of TiO_2 with the prominent peak for (110) direction.

of the C1s peak to 284.8 eV. The spectral positions of the peaks corresponding to Ti2p3/2 and Ti2p1/2 are in line with literature and an expected spin orbit splitting of 5.7 eV is observed.[31,32] Also, the 1/2 and 3/2 spin-orbit doublet components of the Zn2p spectrum and location of peaks at 1045.24 eV and 1022.18 eV are also consistent with the previous reports.[33] As expected the Zn2p peak intensities are intensified by increased number of ALD cycles, which are quite symmetric and have uniform bonding states. In addition, the Ti2p peak widening after 4 cycles is due to chemical state mixing at TiO_2-ZnO interface,[34] see Fig. S1a. To confirm the formation of ZnO film, the surface elemental compositions are detected in which the ratio of Zn in the composite increases by additional ALD cycles of ZnO as expected (Table S1).

In addition to this, to probe surface properties of the structure, investigations on the existence of the surface defects are conducted via analyzing O1s spectra for all samples. In the core-level spectrum of O1s from TiO_2-ZnO core-shell, the spectra can be deconvoluted into 3 peaks, as shown in Fig. 3a. The major peak centered at 530 eV can be assigned to lattice oxygen bond to Ti^{+4} ions in TiO_2 (L_O). Other 2 peaks with binding energies located at 531.4 eV and 532.4 eV are attributed to oxygen vacancies or defects (V_O) and chemisorbed or dissociated oxygen species (C_O) on TiO_2 surface.[35,36] It should be noted that the L_O, V_O and C_O peaks for ultrathin ZnO shell layer are also located at the same binding energies.[37,38] (it is expected that physically adsorbed hydroxyl groups can be easily removed under the ultrahigh vacuum condition of XPS system[39]). Therefore, considering the fact that both TiO_2 and ZnO typically constitute oxygen related defects, it is assumed that no new Gaussian component is added for ZnO coated samples and for all samples fitting was carried out by 3 independent Gaussian functions.

Results from Fig. 3a illustrate that for bare TiO_2 sample oxygen-defect regions are present in the surface layer but no peak is related to C_O species (its peak value is roughly 4 orders of magnitudes smaller than V_O related peak). By deposition of 1 cycle ZnO layer on TiO_2 core, the concentration of defect states is reduced sharply and in the meantime the small shoulder at 532.4 eV is observed. It proves that TiO_2 surface is partially coated with hydroxyl groups (i.e, -OH, H_2O) which are strongly bound to the surface defects. Shifting to thicker layers of ZnO shell, the area related to V_O shows a nearly constant feature while the concentration of C_O radicals rises almost linearly. C_O peak is becoming more significant for 10 cycles coated

sample. As already mentioned, for the surface modification of TiO_2 NWs, ALD method is employed. In ALD process of ZnO, at first, substrate is exposed to the gaseous precursor molecule of water vapor. According to the calculation of free energy in the classical nucleation theory, most of the water-derived hydroxyl groups such as OH radicals and H_2O will be chemisorbed near the imperfections such as defects (like V_O levels) or grain boundaries and smaller concentration on Ti_{5C} sites away from the vacancies.[40–43] Therefore, at the position of oxygen vacancy, Ti atoms presented at the TiO_2 surface make bonds to the water induced hydroxyl groups and subsequently water-induced H ion is chemisorbed on neighbor bridging oxygen atoms[44,45] (The schematic of these process are shown in Fig. 3c). Consequently, it is expected that the ZnO shell layer can passivate (or fill) oxygen vacancy defects by adding an oxygen-containing molecule attached on the surface of TiO_2. Furthermore, it introduces new trapping sites due to adsorbed hydroxyl groups. A better qualitative comparison among different samples can be attainable by determining the relative areas under each Gaussian component. In this sense, the ratio of the areas associated with V_O and C_O peaks to total area of O1s spectrum would be elucidative in Fig. 3b. The sum of these ratios is also provided in the same figure.

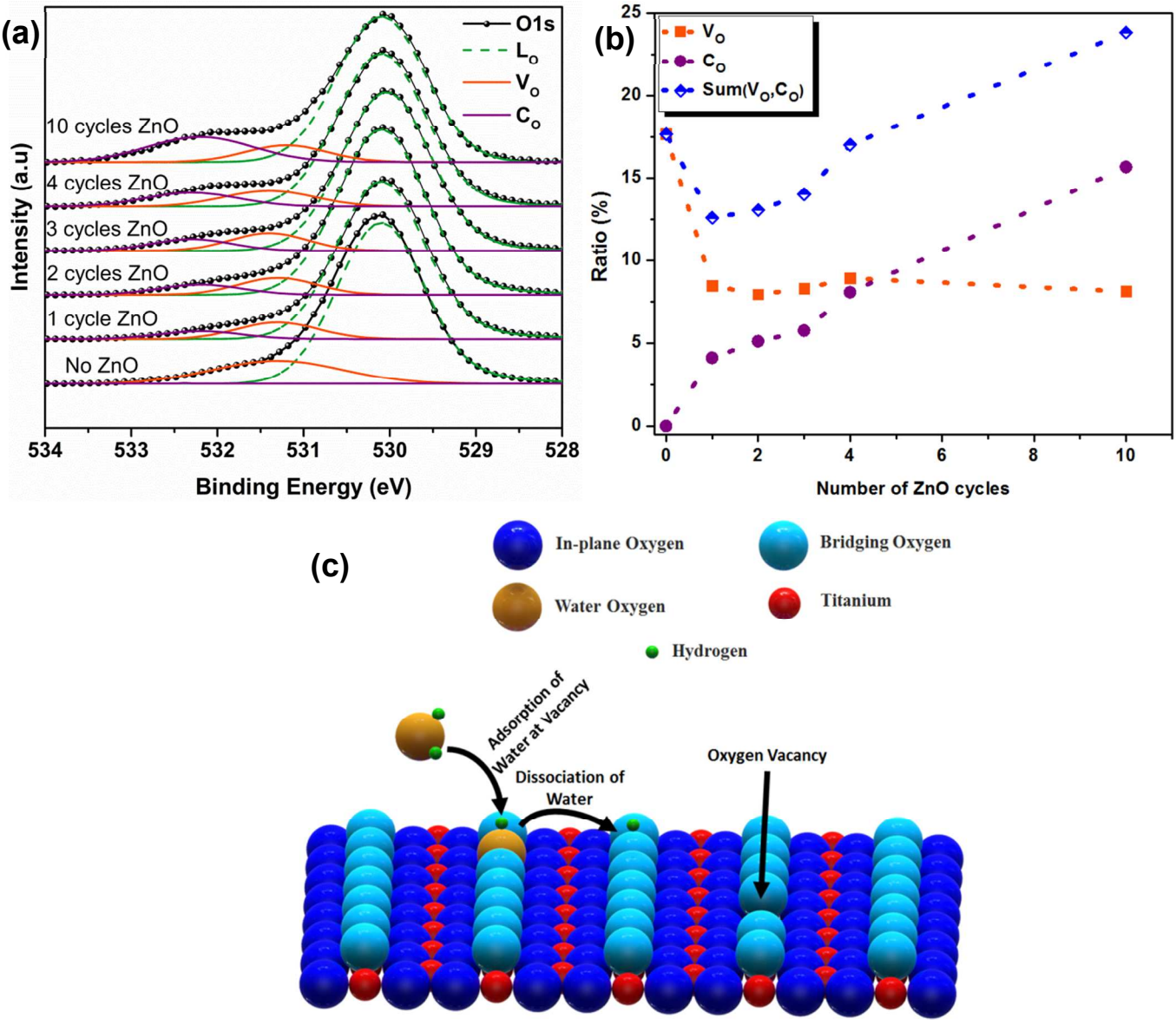

Fig. 3 (a) Core-level XPS spectra of O1s from different ALD cycles coated TiO_2 deconvoluted to three different peaks indicating the presence of three types of oxygen, lattice oxygen (L_O), oxygen vacancy (V_O) and chemisorbed oxygen (C_O) (b) the ratio of the areas associated with V_O and C_O peaks to total area of O1s in which the concentration of V_O defect states stays almost constant after one cycle deposition of ZnO while C_O follows an upward trend (c) depiction of the mechanisms associated with water adsorption and dissociation.

As it can be clearly seen, sum of two ratios has a minimum amount at 1 cycle where together with efficient passivation of V_O defect states, the concentration of C_O species is also sufficiently low. As the thickness of ZnO shell layer increases, the proportion of sum (V_O, C_O) and C_O shows a similar increasing trend.

The PV performances of DSSC devices based on core-sheath composite photoanodes for different ALD cycles of ZnO are evaluated by a Keithley 2400 source meter equipped with a Newport 67005 solar simulator and air mass filter (AM 1.5 G) under a simulated solar light irradiation with an intensity of 100 mW/cm^2. All related parameters including the short-circuit current (J_{sc}), the fill factor (FF), and overall conversion efficiency (η) are summarized in Table 1 and Fig. 4a shows the current density-voltage (J-V) characteristics for these cells. As it can be clearly seen, J_{sc} increases with the subsequent ALD cycles and exhibit the highest by 8.826 mA/cm^2 at 2 cycles. Afterward, it decreases sharply to a relatively low amount of 1.652 mA/cm^2 at 10 cycles. On the other hand, V_{oc} monotonically increases after 2 cycles and reaches to 0.77 V at 10 cycles, for which the performance is poorest. Overall, 2 ALD cycles of ZnO coated TiO_2 NWs exhibits the best conversion efficiency of 3.03% (J_{sc}=8.826 mA/cm^2, FF=0.49) which is nearly tripled compared to that of the TiO_2-only DSSC with nominal efficiency of 1.12% (J_{sc}=3.643 mA/cm^2, FF=0.43). By noting that J_{sc} is mainly determined by light absorption strength over the solar spectrum, the substantial increase in J_{sc} can be understood by investigating spectral incident photon-to-current conversion efficiency (IPCE) measurement results, see Fig. 4b. These results imply that for

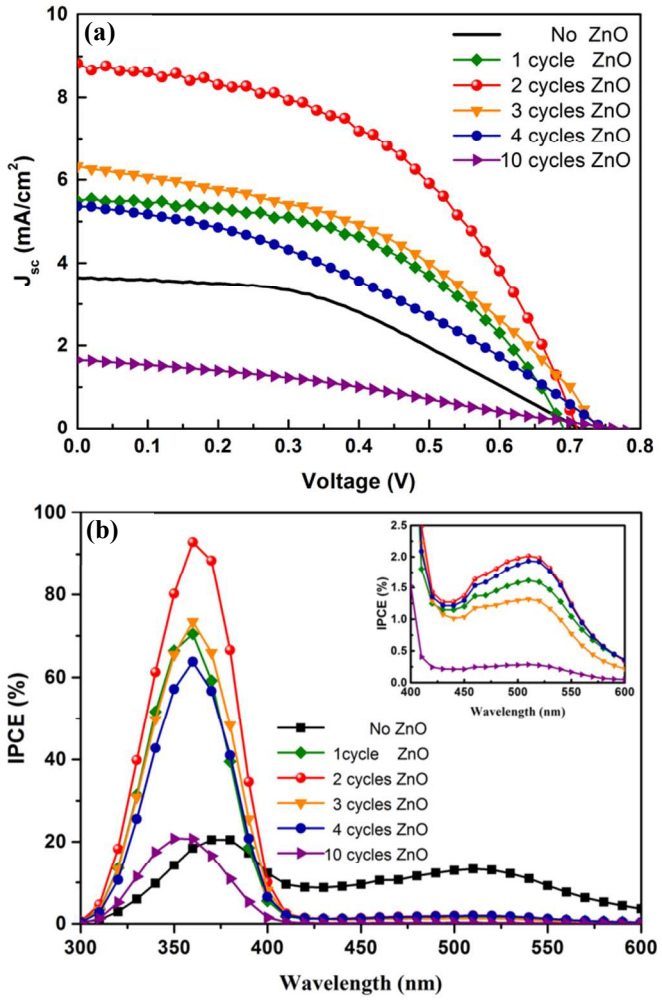

Fig. 4 PV parameters dependence on the ZnO deposition cycles on TiO_2 NWs in DSSC. (a) J -V curves and (b) The IPCE for the DSSCs consisting of the bare TiO_2 and ZnO coated TiO_2 core-shell composite photoanodes. The inset shows magnified image of the IPCE for wavelengths in the range of 400-600 nm.

samples with sub-nanometer ZnO interfacial layer, a giant enhancement of UV light absorption can be observed, while IPCE at visible range has virtually diminished for coated samples.[46] We will discuss later that this quenching in IPCE at visible wavelengths is mainly attributed to conduction band alignment at core-sheath design in which photogenerated electrons are captured at ZnO layer while injecting through the interface.

To gain better insight on electron injection capability of devices, the mechanisms related to photoexcited electrons injection into the conduction band of the photoanode is explored. Injection efficiencies of the devices with 0, 2 and 10 cycles of ALD ZnO shell are investigated using time-resolved single photon counting (TRSPC) as proposed by Koops et al[47], by monitoring the excited state emission decay of the adsorbed dye, (Supporting Information, Fig. S2). This figure shows that by deposition of ALD interfacial ZnO layer, emission decay is gradually delayed. The long-lived excited state of photogenerated electrons illustrates that ZnO layer does slow down injection kinetics of photoinduced electrons through the interface. So this loss should be somehow compensated by retardation in recombination kinetics of the injected electrons at the interface or by suppressing the activity of surface trap states at TiO_2 surface. In other words, an optimized thickness of ZnO overlayer can yield to an enhanced efficiency by providing an effective balance between injection and recombination.

TABLE 1. J–V parameters for the experimental devices with different ZnO ALD cycles under AM 1.5 G filtered spectral illumination at an incident intensity of 100 mW/cm^2.

# of ZnO ALD cycles	Voc (V)	Jsc (mA/cm^2)	FF	η(%)
0	0.71	3.643	0.43	1.12
1	0.70	5.500	0.49	1.90
2	0.70	8.826	0.49	3.03
3	0.73	6.333	0.44	2.04
4	0.75	5.367	0.36	1.43
10	0.77	1.652	0.31	0.40

Reference = 0 cycle. Values given are mean values of 4 cells prepared in a similar way. Experimental errors of the mean values are within ± 10 mV for V_{oc}, ± 0.20 mA/ cm^2 for J_{sc} and ±0.5 % for FF.

Keeping previous results in mind, it should be noted that the mobility of the carriers in organic semiconductors is very sensitive to surface traps [48] in which such defect states can reduce collection efficiency of the device through the trapping of injected electrons. On the other hand, based on XPS results obtained in the previous section, it is expected that ALD deposited ZnO layer passivates surface defects on TiO_2 NWs surface; thus, reduces the electron–hole (e-h) recombination during the charge carrier transport to the electrodes.[49] To further evaluate, the passivation effectiveness of this ultrathin ZnO sheath, photoluminescence (PL) measurement for TiO_2-ZnO core-shell photoanodes is carried out at room temperature for an excitation wavelength of 320 nm. Consistent with XPS results, as seen in Fig. 5, PL spectra for all samples show a near band-edge emission (NBE) at 408 nm arising from e-h recombination across the conduction band (CB) and valance band (VB) of TiO_2, while a smaller peak associated with shallow surface defect traps emission (STE) is centered at 424 nm. The positions of peaks are consistent with previous reports.[50] As it is well known, these surface defects are mainly due to oxygen vacancies and Ti interstitials. O1s spectra for all samples show a small peak indicating the existence of oxygen vacancies in which this V_O energy levels

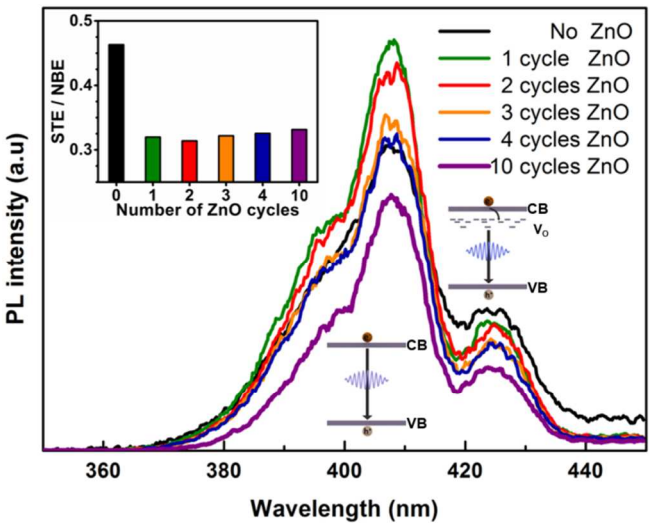

Fig. 5 The PL spectra for different ZnO cycles coated TiO_2 NWs samples for an excitation wavelength of 320 nm. All samples show a near band-edge emission (NBE) at 408 nm arising from e-h recombination across the conduction band (CB) and valance band (VB) of TiO_2 and a shallow surface defect traps emission (STE) centered at 424 nm. The inset shows the ratio of STE / NBE.

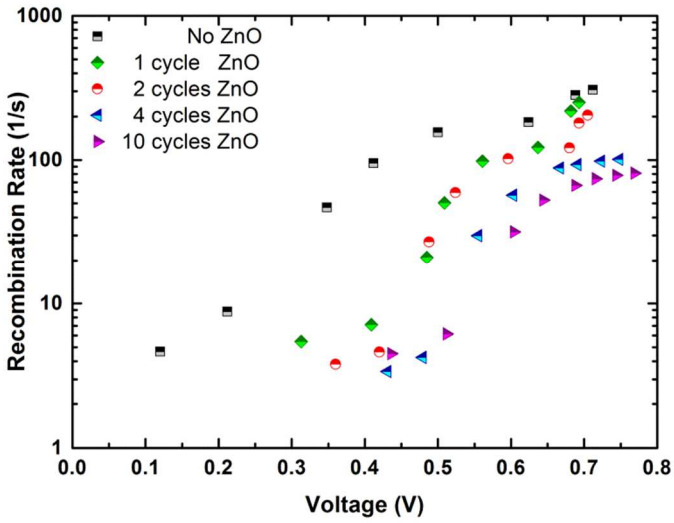

Fig. 6 Electron recombination rates for different DSSC devices including bare and different ALD ZnO cycles coated TiO_2 NWs obtained from transient photovoltage decay measurement.

forms a shallow donor state below the CB of TiO_2.[51] With this in mind, other possible surface defects can be related to Ti interstitials which are fully ascribed to oxygen vacancies. This is because, in an ionic scheme, it is likely that two excess electrons per V_O can be transformed to the nearest neighboring Ti atoms and cause redistribution of excess charges.[52] However, no trace associated with Ti interstitial in Ti2P spectra was found. Therefore, the dominant surface traps in our samples are attributed to V_O trap states. Coming back to the PL results, compared to unpassivated sample, passivation of NWs with a couple of ALD ZnO cycles intensifies the NBE peak. From Fig. 5, deposition of 1 cycle of interfacial ZnO layer has strengthened this peak along passivation of surface traps of TiO_2, but a further increase on shell thickness leads to a reduction of PL intensity. A possible explanation regarding this reduction for thicker ZnO shell layers is hidden in XPS measurement results. As it is explained in Fig. 3b, although deposition of first ALD cycles of ZnO passivates oxygen vacancy related surface defects, for subsequent cycles the amount of chemisorbed oxygen on the core-sheath surface follows an upward trend. Based on Madelung potential of the highly ionic crystal, these oxygen-containing molecules will act as a new trap states in the core-shell structure.[37,44] Therefore, these chemisorbed oxygen radicals can be helpful for providing an efficient charge separation in a way that some of the photoexcited electrons migrate to this localized trapping hosts. This separation is responsible for reduction in NBE intensity due to reducing the probability of e-h recombination across the band gap. On the other hand, STE for all passivated samples exhibit a gradual quenching effect and this effect is more pronounced as moving to thicker shell layer. Considering that the origin of STE is generally attributed to intrinsic V_O surface defects of TiO_2, these results strongly suggest that there is an association between passivation of non-radiative recombination sites by ultrathin ZnO and the increment in NBE emission intensity simultaneously quenching STE. Besides this, to provide a qualitative comparison, the intensity ratio of STE/NBE is calculated for all samples (the inset of Fig. 5). From this data, it is apparent that the ratio decreases considerably for 1 cycle ZnO coated sample and stays almost constant for thicker layers which is in line with XPS measurement results.

Further understandings of the impact of ZnO layer on PV properties of devices are pursued with transient photovoltage decay measurement. This measurement is a useful technique to understand the charge recombination rate at TiO_2-electrolyte interface. Fig. 6 illustrates the recombination rates extracted from photovoltage decay measurement for different steady-state light biases conditions. As depicted in this graph, recombination rate for all passivated samples are lower than that of the reference cell. Since the recombination rate is related to retardation of electrons' back-transfer, in order to slow down this kinetics effectively, the conduction band position of shell layer should be several electron volts above (at more negative potential) than that of TiO_2 core. However, it will be shown that the conduction band position of ZnO layer is below that of TiO_2 core. Hence, this retardation in electrons' back transfer rate should be attributed to a ZnO induced modification on TiO_2 surface. According to previous studies, the oxygen-containing gas molecules tend to be chemisorbed on the host materials surface via capturing free electrons.[36,40,41,44] As a result, these chemisorbed oxygen radicals will reduce free carriers density in the vicinity of the surface and deplete the surface electron states.[53,54] This triggers the formation of the space charge region and the band bending near the NWs surface. Looking back to the XPS results, it can be found that density of chemisorbed oxygen pursues an increasing trend while moving to thicker ZnO shell layer. So, it is speculated that ZnO induced surface band bending (SBB) will be more pronounced for subsequent ALD cycles. It should be noted that injected electrons' back-reactions are mainly via two routes 1) a direct recombination among CB or 2) exponentially distributed traps mediated electrons with oxidized redox couple. Therefore, the ZnO shell layer will reduce both recombination rates (K^{CB}_{ET} and K^{trap}_{ET}) through inducing an effective SBB at the TiO_2 surface and reducing surface traps density at the interface, respectively. Keeping this in mind, first cycles of ZnO layer will reduce recombination rates just due to passivation of surface traps, but moving to greater cycles SBB effect will also be added to the earlier one. Consequently, more efficient reduction in recombination rate of injected electrons will be provided.

In addition to suppressing recombination of photogenerated electrons across the interface, ZnO shell layer can contribute in device performance enhancement by modifying NWs surface owing to its high isoelectric point (IEP of ZnO is 9 compared to 5 for TiO_2[24]) IEP defines the PH at which the oxide surface has a net zero charge[55]. ZnO layer, as an alkali material with a PH>7, will be

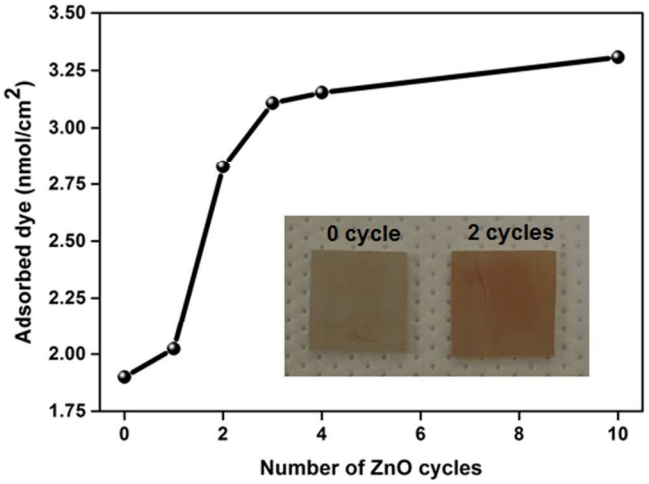

Fig. 7 The amounts of dye adsorbed on the surface of different number of ALD ZnO cycles coated TiO_2 NWs showing a sharp increase in 2 cycles coated sample. For subsequent cycles, this amount follows a gradual increase.

positively charged, and hence it will become a more favorable host site for acidic carboxylic chains of N719 (PH<7). Therefore, the dye adsorption is expected to be increased by introduction of ZnO layer. To substantiate this claim, dye adsorption measurement is utilized by Microplate Reader (Spectramax M5) to explore its trend as a function of number of ALD cycles. The amount of dye adsorbed on the photoanode is calculated after desorption of N719 dye from the surface by 1:1 ethanol–0.1 M NaOH solution and it is shown in Fig. 7 (Details of the measurement is explained in Supporting Information Fig. S3-S4). While, the first cycle of ZnO causes a small increase in dye uptake compared to bare TiO_2 layer, it is well-known that the monolayer usually cannot reach 100% coverage. It is apparent from Fig. 7, there is a significant enhancement in the amount of dye adsorbed at two cycles. After two cycles, adsorption profile follows a gradual raise as expected.

As it was mentioned earlier, in the case of two cycles, ZnO passivation layer increases power conversion efficiency up to a maximum and then it falls back to extreme low efficiencies at 10 cycles coated sample. In order to scrutinize physical reasons responsible for this exponential drop in device performance, it is imperative to understand electron injection kinetics at the interface. For this purpose, understanding the band alignment at the heterostructure interface can provide better insight on the device performance. Although some papers report a band alignment in which the position of conduction band of ZnO layer is in higher energies than that of TiO_2[56–58], some others show the vice versa[59–61]. Considering this fact, we first adopted a high resolution XPS measurement to explore the band alignment of TiO_2-ZnO core-sheath structure. To understand electron flow process and charge transfer in the structure, valence and conduction band offsets ((ΔE_V) and (ΔE_C)) of structure are determined by well-established analysis technique of Kraut et. al.[62] In this approach, ΔE_{CL} is the energy difference between Zn2p and Ti2p core levels (CLs) in the TiO_2-ZnO (heterojunction) sample as it is shown in Fig. S5 and found as 563.57 eV (also see Equation 1[63]). On the other hand, $(E_{CL} - E_{VBM})_{TiO_2}$ is the energy difference of the CL to valance band maximum (VBM) for rutile TiO2 NWs and it is determined as 456.09 eV from Fig. S6. Whereas for ZnO, $(E_{CL} - E_{VBM})_{ZnO}$ is found to be 1018.96eV. It should be noted that the CL spectra of Zn 2p3/2 and Ti 2p3/2 show peaks located at 1021.58 eV and 458.68 eV, respectively. In this regard, the values of E_{VBM} are calculated to be 2.62 eV for rutile TiO_2 (which is in good agreement with[64]) and 2.59 eV for ZnO, see Fig. S6. All obtained data are summarized in Table 2. The optical band gap of the bare rutile TiO2 NW arrays is also found to be 3.02 eV[65] which is estimated from the graph of $(\alpha h\nu)^{1/2}$ versus $h\nu$, see Fig. S7. The band gap of ZnO is taken as 3.37 eV at room temperature[66]. Finally, ΔE_V and ΔE_C are calculated from Equations 2-3 and found to be 0.7 eVand 0.35 eV, respectively.

$$\Delta E_{CL} = \left(E_{Zn} - E_{TiO_2}\right)_{\text{TiO2/ZnO core/shell}} \quad (1)$$

$$\Delta E_V\left(\frac{\text{ZnO}}{\text{TiO}_2}\right) = (E_{CL} - E_{VBM})^{\text{bulk}}_{\text{TiO}_2} - (E_{CL} - E_{VBM})^{\text{bulk}}_{\text{ZnO}} + \Delta E_{CL} \quad (2)$$

$$\Delta E_C = \left(E_{g_{TiO2}} - E_{g_{ZnO}} + \Delta E_V\right)_{\text{TiO2/ZnO core/shell}} \quad (3)$$

According to these calculations, an energy band diagram of the structure is expected as shown in Fig. 8 in which conduction band edge of rutile TiO_2 is 0.35 eV above that of ZnO. This band alignment would persuade ZnO interfacial layer to act as a quantum well to capture photogenerated dye electrons.[57]

TABLE 2. Results obtained from XPS valence band spectra

Sample	Region	Binding Energy(eV)
TiO_2	Ti $2p^{3/2}$	458.68
	VBM	2.59
ZnO	Zn $2p^{3/2}$	1021.58
	VBM	2.62
TiO_2 /ZnO	Zn $2p^{3/2}$	1022.18
	Ti $2p^{3/2}$	458.61

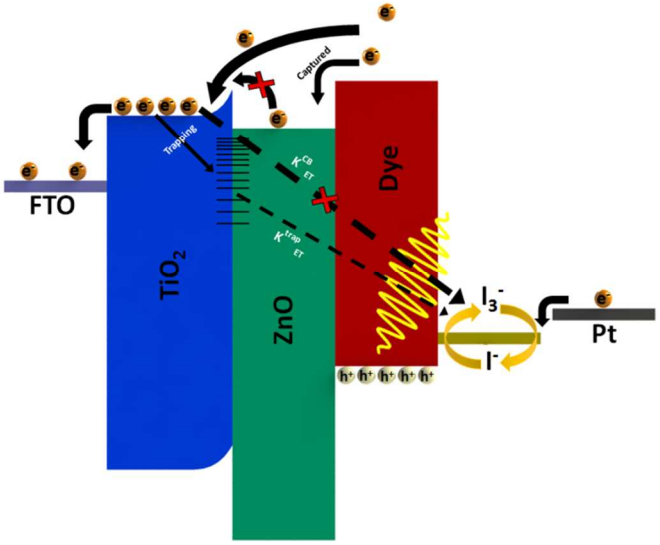

Fig. 8 Energy band diagram of DSSC showing band alignment in the TiO_2-ZnO interface. A part of photoexcited electrons will be captured by ZnO well while the rest of electrons will be injected to CB of TiO_2. ZnO passivation layer will reduce recombination rates through reduction in surface trap states at the interface and inducing surface band bending at the TiO_2 surface.

Whether photogenerated dye electrons will be captured by the potential well or will escape from it, depends on well-width and initial kinetic energy of electrons which is related to incident photon energy.[67] By going toward to thicker ZnO layers the probability that an electron is being captured increases. Hence the amount of electrons captured in the well will be exponentially increased and short circuit current will show a significant reduction. On the other hand, for photogenerated electron at lower photon energies, it is more likely that an electron will diffuse into the ZnO potential well during thermalization towards the TiO_2 conduction band.

III. Conclusions

In conclusion, we demonstrate that by surface engineering of TiO_2 NWs based photoanode using an optimized sub-nanometer thick (2 cycles) ALD-coated ZnO interfacial sheath layer, device efficiency is boosted about 3 times compared to reference device in the absence of ZnO shell layer. The presented results and strategy affirms that adding angstrom thick ZnO layer to the TiO_2 NWs surface can improve the cell efficiency by introducing an effective reduction of density of surface trap states together with increasing the amount of dye uptake. As explained, although such layer can cause retardation in recombination kinetics for back-transfer of electrons at the interface, thicker layers hamper the injection rate of electrons. The obtained results in this paper serve a promising improvement in a wide range of applications based on TiO_2 NWs such as photovoltaic and photocatalytic applications in which such an ultrathin passivation layer can reduce recombination rate without affecting the injection kinetics and diffusion of minority carriers due to its negligible thickness.

IV. Experimental Section

Ethanol, acetone, titanium butoxide ($Ti(OCH_2CH_2CH_2CH_3)_4$) (97%) and hydrochloric acid HCl (36%) are all from Sigma–Aldrich Co and used as received. FTO coated glass (7 Ω sq-1), photosensitizer dye Ruthenizer 535-bis TBA (N719), Iodalyte HI electrolyte are all purchased from Solaronix. For ZnO deposition by ALD, diethylzinc ($(C_2H_5)_2Zn$ or DEZn, Sigma-Aldrich) and HPLC-grade water (H_2O) are used as the zinc and oxygen precursors, respectively.

TiO_2 NWs are prepared on FTO glass based on hydrothermal technique. First, FTO glasses are ultrasonically cleaned for 15 min sequentially by using ethanole; acetone and de-ionized (DI) water and then dried by N_2 flow. Concentrated HCl (20 ml) and DI water (20 ml) are mixed in a teflon-lined stainless steel autoclave (45 ml) for 10 min and afterward 0.8 ml titanium butoxide is added. The mixture is stirred for an additional 30 min under ambient conditions. FTO is placed into solution with the conducting side facing up with 45° angle against the autoclave wall. The hydrothermal reaction is performed at 140 °C for 4 hours in an oven. Prior to taking out, the FTO glass is cooled to room temperature in air inside the autoclave. The NWs then rinsed extensively with DI water and dried in air.

Finally NWs are coated with ZnO by ALD reactor (Cambridge Nanotech Savannah S100). The substrate temperature was kept at 250 °C during the ALD process using DEZn at 80 °C and distilled water. The pulse and purge time for both is kept to be 0.015s and 10s, respectively. The deposition was carried out using successive different cycles (1, 2, 3, 4, 10) of ZnO as an ultrathin layer on TiO_2 NW arrays with the estimated growth rate 1.3 Å per cycle. The ZnO coated TiO_2 NWs are kept at 80 °C for 15 minutes before being soaked in 0.5 mmol N719 in a t-butanol/acetonitrile (1:1, in volume ratio) solution, for 24 hours at room temperature. The samples are rinsed with acetonitrile to remove non-chemisorbed dye molecules. The drilled platinum-coated conducting glass is used as counter electrodes bonded to TiO_2 NWs by 25μm-thick thermal sealant (Dupont). The active area of each cell is filled with electrolyte driven by capillary force through the hole. The area of the electrode was controlled using a mask of 0.30 cm^2 area on the hot-melt sealed film.

V. Acknowledgements

This work was supported by the Scientific and Technological Research Council of Turkey (TUBITAK), grant numbers 109E044, 112M004, 112E052 and 113M815. A. K. O. acknowledges a Marie Curie International Reintegration Grant (PIOS, Grant # PIRG04-GA-2008-239444). The authors thank Ph. D. students, Mr. Ruslan Garifullin, Mr. Burak Guzelturk and UNAM technical staff Enver Kahveci and Mustafa Guler.

References

1. O'Regan Brian and M. Gratzel, *Nature*, 1991, **353**, 737–739.
2. A. J. Nozik and J. Miller, *Chem. Rev.*, 2010, **110**, 6443–5.
3. M. Grätzel, *J. Photochem. Photobiol. C Photochem. Rev.*, 2003, **4**, 145–153.
4. N. Arrays, P. Chen, M. Takata, S. Uchida, H. Miura, K. Sumioka, S. M. Zakeeruddin, and M. Gra, 2008, **2**, 1113–1116.
5. J. R. Pitts and B. A. Gregg, 2000, 5626–5630.
6. S. Ito, N.-L. C. Ha, G. Rothenberger, P. Liska, P. Comte, S. M. Zakeeruddin, P. Péchy, M. K. Nazeeruddin, and M. Grätzel, *Chem. Commun. (Camb).*, 2006, 4004–6.
7. Q. Zhang and G. Cao, *Nano Today*, 2011, **6**, 91–109.
8. N. Robertson, *Angew. Chem. Int. Ed. Engl.*, 2006, **45**, 2338–45.
9. C. Klein, M. K. Nazeeruddin, P. Liska, D. Di Censo, N. Hirata, E. Palomares, J. R. Durrant, and M. Grätzel, *Inorg. Chem.*, 2005, **44**, 178–80.
10. D. Kuang, S. Ito, B. Wenger, C. Klein, J.-E. Moser, R. Humphry-Baker, S. M. Zakeeruddin, and M. Grätzel, *J. Am. Chem. Soc.*, 2006, **128**, 4146–54.
11. M. K. Nazeeruddin, P. Péchy, T. Renouard, S. M. Zakeeruddin, R. Humphry-Baker, P. Comte, P. Liska, L. Cevey, E. Costa, V. Shklover, L. Spiccia, G. B. Deacon, C. a Bignozzi, and M. Grätzel, *J. Am. Chem. Soc.*, 2001, **123**, 1613–24.
12. S. Y. Huang, G. Schlichtho, A. J. Nozik, M. Gra, and A. J. Frank, 1997, **5647**, 2576–2582.
13. M. Law, L. E. Greene, J. C. Johnson, R. Saykally, and P. Yang, *Nat. Mater.*, 2005, **4**, 455–9.
14. J. Van De Lagemaat, N. Park, and A. J. Frank, 2000, 2044–2052.

15. C. P. Grigoropoulos and H. J. Sung, 2011, 666–671.

16. S. H. Ko, 2014, **2**, 54–62.

17. M. J. Katz, M. J. D. Vermeer, O. K. Farha, M. J. Pellin, and J. T. Hupp, 2013.

18. A. R. Pascoe, L. Bourgeois, N. W. Du, W. Xiang, and Y. Cheng, 2013.

19. T. P. Brennan, J. T. Tanskanen, K. E. Roelofs, J. W. F. To, W. H. Nguyen, J. R. Bakke, I. Ding, B. E. Hardin, A. Sellinger, M. D. Mcgehee, and S. F. Bent, 2013.

20. E. Palomares, J. N. Clifford, S. a Haque, T. Lutz, and J. R. Durrant, *J. Am. Chem. Soc.*, 2003, **125**, 475–82.

21. A. K. Chandiran, N. Tetreault, R. Humphry-Baker, F. Kessler, E. Baranoff, C. Yi, M. K. Nazeeruddin, and M. Grätzel, *Nano Lett.*, 2012, **12**, 3941–7.

22. A. K. Chandiran, M. K. Nazeeruddin, and M. Grätzel, *Adv. Funct. Mater.*, 2014, **24**, 1615–1623.

23. T. C. Li, S. Go, F. Fabregat-santiago, J. Bisquert, P. R. Bueno, C. Prasittichai, J. T. Hupp, and T. J. Marks, 2009, **14**, 18385–18390.

24. Y. Diamant, S. Chappel, S. G. Chen, O. Melamed, and A. Zaban, *Coord. Chem. Rev.*, 2004, **248**, 1271–1276.

25. E. Barea, X. Xu, V. González-Pedro, T. Ripollés-Sanchis, F. Fabregat-Santiago, and J. Bisquert, *Energy Environ. Sci.*, 2011, **4**, 3414.

26. A. Kay, M. Gra, and D. C. S. Nanocrystals, 2002, 2930–2935.

27. Z. L. Wang, *Annu. Rev. Phys. Chem.*, 2004, **55**, 159–96.

28. R. H. Baughman, A. a Zakhidov, and W. a de Heer, *Science*, 2002, **297**, 787–92.

29. Z. W. Pan, Z. R. Dai, and Z. L. Wang, 2001, **291**, 2000–2002.

30. H. Ceylan, C. Ozgit-Akgun, T. S. Erkal, I. Donmez, R. Garifullin, A. B. Tekinay, H. Usta, N. Biyikli, and M. O. Guler, *Sci. Rep.*, 2013, **3**, 2306.

31. S.-C. Li and U. Diebold, *J. Am. Chem. Soc.*, 2010, **132**, 64–6.

32. M. Andersson and O. Lars, 2002, 10674–10679.

33. S. Kwon, S. Bang, S. Lee, S. Jeon, W. Jeong, H. Kim, S. C. Gong, H. J. Chang, H. Park, and H. Jeon, *Semicond. Sci. Technol.*, 2009, **24**, 035015.

34. A. R. González-elipe, 2001, **2**.

35. D. Chu, A. Younis, and S. Li, *J. Phys. D. Appl. Phys.*, 2012, **45**, 355306.

36. F. Kayaci, S. Vempati, C. Ozgit-Akgun, I. Donmez, N. Biyikli, and T. Uyar, *Nanoscale*, 2014.

37. X. Zhang, J. Qin, Y. Xue, P. Yu, B. Zhang, L. Wang, and R. Liu, *Sci. Rep.*, 2014, **4**, 4596.

38. X.-G. Han, H.-Z. He, Q. Kuang, X. Zhou, X.-H. Zhang, T. Xu, Z.-X. Xie, and L.-S. Zheng, *J. Phys. Chem. C*, 2009, **113**, 584–589.

39. R. Wang, N. Sakai, A. Fujishima, and T. Watanabe, 1999, 2188–2194.

40. P. Scheiber, A. Riss, M. Schmid, P. Varga, and U. Diebold, *Phys. Rev. Lett.*, 2010, **105**, 216101.

41. S. Tan, Y. Ji, Y. Zhao, A. Zhao, B. Wang, J. Yang, and J. G. Hou, *J. Am. Chem. Soc.*, 2011, **133**, 2002–9.

42. N. G. Petrik and G. a Kimmel, *Phys. Chem. Chem. Phys.*, 2014, **16**, 2338–46.

43. C. Lun Pang, R. Lindsay, and G. Thornton, *Chem. Soc. Rev.*, 2008, **37**, 2328–53.

44. F. Liu, L. Lu, P. Xiao, H. He, L. Qiao, and Y. Zhang, 2012, **33**, 2255–2259.

45. N. Bundaleski, a G. Silva, U. Schröder, a M. C. Moutinho, and O. M. N. D. Teodoro, *J. Phys. Conf. Ser.*, 2010, **257**, 012008.

46. J. Wu, G. Yue, Y. Xiao, J. Lin, M. Huang, Z. Lan, Q. Tang, Y. Huang, L. Fan, S. Yin, and T. Sato, *Sci. Rep.*, 2013, **3**, 1283.

47. S. E. Koops, B. C. O'Regan, P. R. F. Barnes, and J. R. Durrant, *J. Am. Chem. Soc.*, 2009, **131**, 4808–18.

48. L. Zhao, M. Xia, Y. Liu, B. Zheng, Q. Jiang, and J. Lian, 2012, **53**, 463–468.

49. Z. W. Ai, Y. Wu, H. Wu, T. Wang, C. Chen, Y. Xu, and C. Liu, *Nanoscale Res. Lett.*, 2013, **8**, 105.

50. S. Mathew, A. K. Prasad, T. Benoy, P. P. Rakesh, M. Hari, T. M. Libish, P. Radhakrishnan, V. P. N. Nampoori, and C. P. G. Vallabhan, *J. Fluoresc.*, 2012, **22**, 1563–9.

51. M. K. Nowotny, L. R. Sheppard, T. Bak, and J. Nowotny, 2008, 5275–5300.

52. G. Liu, F. Li, D.-W. Wang, D.-M. Tang, C. Liu, X. Ma, G. Q. Lu, and H.-M. Cheng, *Nanotechnology*, 2008, **19**, 025606.

53. T. T. Pham, K. Y. Lee, J.-H. Lee, K.-H. Kim, K.-S. Shin, M. K. Gupta, B. Kumar, and S.-W. Kim, *Energy Environ. Sci.*, 2013, **6**, 841.

54. C.-Y. Chen, J. R. D. Retamal, I.-W. Wu, D.-H. Lien, M.-W. Chen, Y. Ding, Y.-L. Chueh, C.-I. Wu, and J.-H. He, *ACS Nano*, 2012, **6**, 9366–72.

55. B. Tadesse, 1997.

56. K. Shen, K. Wu, and D. Wang, *Mater. Res. Bull.*, 2014, **51**, 141–144.

57. S. Xuhui, C. Xinglan, T. Wanquan, W. Dong, and L. Kefei, *AIP Adv.*, 2014, **4**, 031304.

58. C. Cheng, A. Amini, C. Zhu, Z. Xu, H. Song, and N. Wang, *Sci. Rep.*, 2014, **4**, 4181.

59. M. Law, L. E. Greene, A. Radenovic, T. Kuykendall, J. Liphardt, and P. Yang, *J. Phys. Chem. B*, 2006, **110**, 22652–63.

60. R. A. Rakkesh and S. Balakumar, *J. Nanosci. Nanotechnol.*, 2013, **13**, 370–376.

61. Y. Xu, M.A. A. Schoonen, Am. Mineral. 2000, 85, 543−556.

62. S. P. Kowalczyk, 1983, **28**.

63. R. Deng, B. Yao, Y. F. Li, Y. M. Zhao, B. H. Li, C. X. Shan, Z. Z. Zhang, D. X. Zhao, J. Y. Zhang, D. Z. Shen, and X. W. Fan, *Appl. Phys. Lett.*, 2009, **94**, 022108.

64. D. O. Scanlon, C. W. Dunnill, J. Buckeridge, S. a Shevlin, A. J. Logsdail, S. M. Woodley, C. R. a Catlow, M. J. Powell, R. G. Palgrave, I. P. Parkin, G. W. Watson, T. W. Keal, P. Sherwood, A. Walsh, and A. a Sokol, *Nat. Mater.*, 2013, **12**, 798–801.

65. F.-X. Xiao, J. Miao, and B. Liu, *Mater. Horizons*, 2014, **1**, 259.

66. L. E. Aygun, F. B. Oruc, F. B. Atar, and a. K. Okyay, *IEEE Photonics J.*, 2013, **5**, 2200707–2200707.

67. A. Belsky, K. Ivanovskikh, A. Vasil'ev, M.-F. Joubert, and C. Dujardin, *J. Phys. Chem. Lett.*, 2013, **4**, 3534–3538.

Table of Contents Graphic

Surface Engineered Angstrom Thick ZnO-sheathed TiO_2 Nanowires as Photoanode for Performance Enhanced Dye-sensitized Solar Cells

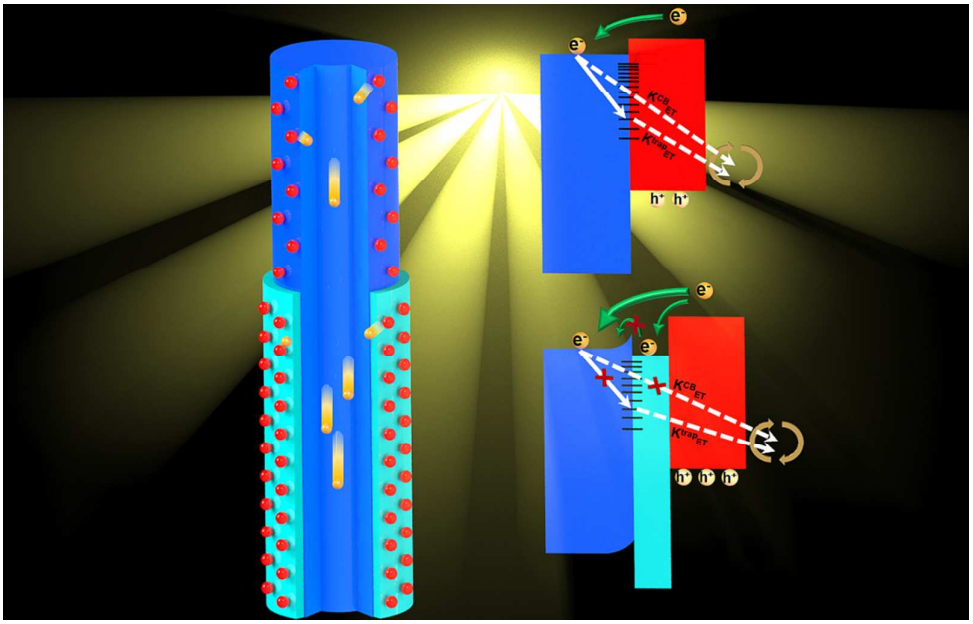

Magnified Version of TOC